

1 Natural Marine Cloud Brightening in the Southern Ocean

2
3 Gerald G. Mace¹, Sally Benson¹, Ruhi Humphries^{2,3}, Peter M. Gombert¹, Elizabeth
4 Stern¹

5
6 ¹Department of Atmospheric Sciences, University of Utah, Salt Lake City, Utah, United
7 States of America

8 ²Climate Science Centre, CSIRO Oceans and Atmosphere, Melbourne, Australia

9 ³Australian Antarctic Program Partnership, Institute for Marine and Antarctic Studies,
10 University of Tasmania, Hobart, Tasmania, Australia

11 Corresponding Author Information:

12 Gerald "Jay" Mace, Professor

13 Department of Atmospheric Sciences, University of Utah

14 135 South 1460 East Rm 819 (819 WBB)

15 Salt Lake City, Utah, 84112-0110

16 Cell Phone and SMS: +1 801 201 7944

17 Email: jay.mace@utah.edu

18

19

20

21

22 Abstract: The number of cloud droplets per unit volume (N_d) is a fundamentally
23 important property of marine boundary layer (MBL) liquid clouds that, at constant liquid
24 water path, exerts considerable controls on albedo. Past work has shown that regional
25 N_d has direct correlation to marine primary productivity (PP) because of the role of
26 seasonally varying biogenically-derived precursor gasses in modulating secondary
27 aerosol properties. These linkages are thought to be observable over the high latitude
28 oceans where strong seasonal variability in aerosol and meteorology covary in mostly
29 pristine environments. Here, we examine N_d variability derived from five years of MODIS
30 level-2 derived cloud properties in a broad region of the summer Eastern Southern Ocean
31 and adjacent marginal seas. We demonstrate latitudinal, longitudinal, and temporal
32 gradients in N_d that are strongly correlated with the passage of air masses over high PP
33 waters that are mostly concentrated along the Antarctic Shelf poleward of 60°S. We find
34 that the albedo of MBL clouds in the latitudes south of 60°S is significantly higher than
35 similar LWP clouds north of this latitude.

36
37 Short Summary: The number cloud droplets per unit volume is a significantly
38 important property of clouds that controls their reflective properties. Computer models of
39 the Earth's atmosphere and climate have low skill at predicting the reflective properties of
40 Southern Ocean clouds. Here we investigate the properties of those clouds using satellite
41 data and find that the cloud droplet number in the Southern Ocean is related to the
42 oceanic phytoplankton abundance near Antarctica and cause clouds there to be
43 significantly brighter than clouds further north.

44
45 1. Introduction

46
47 The cloud and precipitation properties of the Southern Ocean (SO) have received
48 considerable attention since Trenberth and Fasullo (2010) identified a high bias in
49 surface-absorbed solar energy there (McFarquhar et al., 2020). This bias has been
50 traced to erroneously small Marine Boundary Layer (MBL) cloud cover in simulations of
51 the Southern Ocean climate (Bodas-Salcedo, et al., 2016; Naud et al., 2016). The
52 actual SO cloud climatology and associated albedo are dominated by geometrically thin
53 MBL clouds (Mace et al., 2010; Mace et al., 2020, 2021). Because the predominant
54 shallow boundary layer clouds rarely precipitate (Huang et al., 2016), they are sensitive
55 to cloud condensation nuclei (CCN) concentrations (Twohy and Anderson, 2008;
56 Painemal et al., 2017).

57
58 In the SO, the CCN seasonal cycle (Ayers and Gras, 1991; Vallina et al. 2006; Gras and
59 Keywood, 2017) is reflected in basin-wide cloud property variations (Krüger and Graßl,
60 2011). McCoy et al. (2015) and Mace and Avey (2017) also found that MODIS- and A-
61 Train-derived cloud properties over the SO, demonstrate a similar seasonal cycle in
62 cloud droplet number concentration (N_d) as for CCN. The basin wide variability in CCN
63 and cloud albedo have been shown to be correlated with marine primary productivity
64 (PP – defined as the net organic matter, mostly produced by phytoplankton, that is
65 suspended in the ocean; Vallina et al., 2006; Krüger and Graßl, 2011; McCoy et al.,
66 2015). McCoy et al. (2020) argue that the SO can be viewed as an analog of the
67 preindustrial Earth. Given the large natural seasonal variability in CCN and clouds, the

68 SO is a natural laboratory to understand the processes that contribute to simulated
 69 aerosol-related indirect forcing variability in climate models (Carslaw et al. 2013).
 70

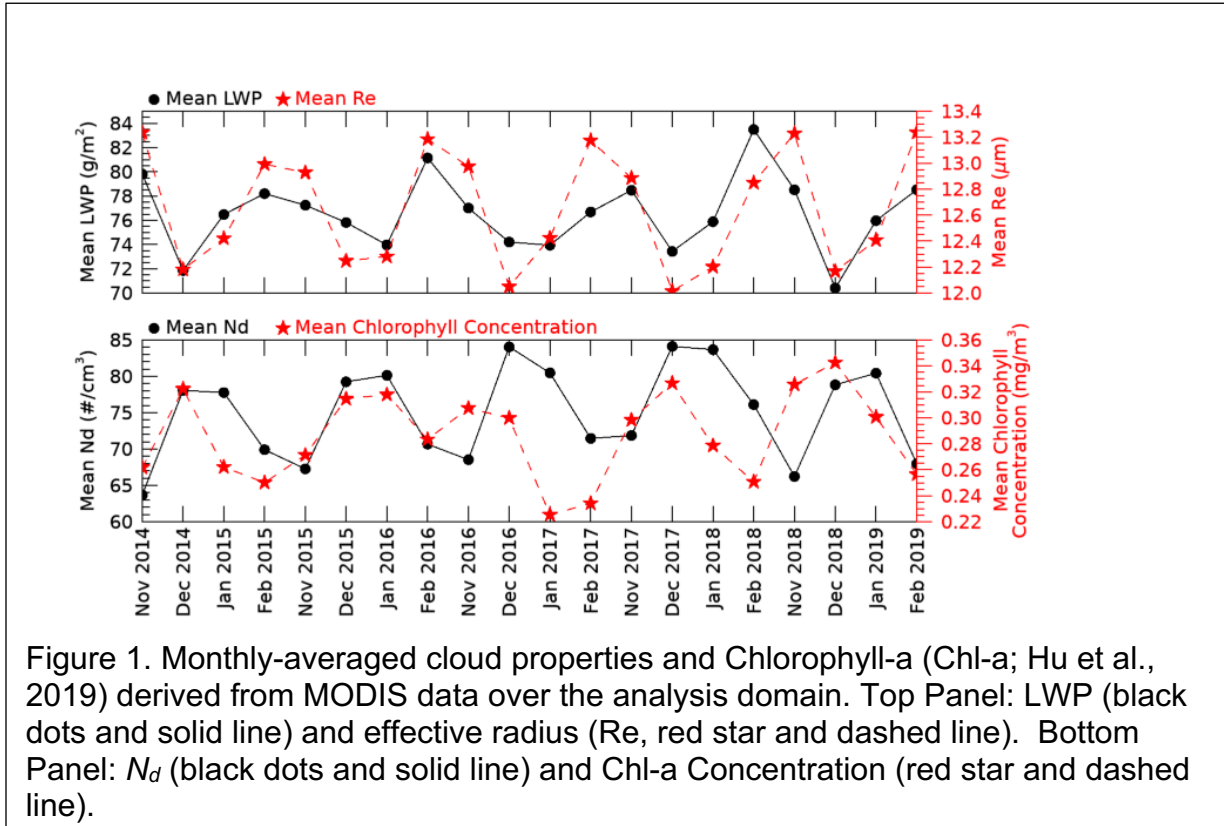


Figure 1. Monthly-averaged cloud properties and Chlorophyll-a (Chl-a; Hu et al., 2019) derived from MODIS data over the analysis domain. Top Panel: LWP (black dots and solid line) and effective radius (Re, red star and dashed line). Bottom Panel: N_d (black dots and solid line) and Chl-a Concentration (red star and dashed line).

71 CCN and cloud droplet N_d in the SO are higher in Summer when significant latitudinal
 72 gradients have been documented in the SO Australasian sector (Humphries et al.,
 73 2021). Using time of flight aerosol chemical speciation monitor (ACSM) and ion
 74 concentrations from filter samples, Humphries et al., (2021) analyzed the covariance of
 75 aerosol chemistry, CCN at 0.5% supersaturation, and Condensation Nuclei (CN) larger
 76 than 10 nm collected aboard Australian research vessels during the 2018 Austral
 77 Summer (McFarquhar et al., 2021). While sulfates were a major compositional
 78 component of aerosol at all latitudes during summer these compounds were in higher
 79 fractional abundance poleward of 65°S where overall CCN numbers were higher by
 80 ~50%. Chloride derived from sea salt was dominant in the region equatorward of 65°S
 81 but was mostly absent south of 65°S. The ratio of CCN to CN at 0.5% supersaturation
 82 increased considerably south of 65°S suggesting unique aerosol chemical processes
 83 compared to the open ocean. Humphries et al. (2021) also discusses how this
 84 compositional boundary in aerosol chemistry is often very distinct in the East Antarctic
 85 waters between 60°S and 65°S. Following Humphries et al. we will refer to this belt as
 86 the Atmosphere Compositional Front of Antarctica (ACFA). Humphries et al. (2021)
 87 conclude that aerosol, newly condensed from gas phase sulfur species such as from
 88 the oxidation of dimethyl sulfide (DMS), are an important component of high latitude
 89 CCN. These products of phytoplankton physiology are released into the atmosphere

90 from the highly productive waters from $\sim 60^{\circ}$ S to the Antarctic – a region well known for
91 a vast marine food web (Deppler and Davidson, 2017; Behrenfeld et al., 2017).
92
93 Mace et al. (2021a) derived N_d and other cloud microphysical properties from non-
94 precipitating stratocumulus clouds using shipborne remote sensing data. They found
95 that stratiform clouds poleward of the ACFA had significantly higher N_d than
96 equatorward. One particular case took place when the Icebreaker Aurora Australis was
97 at the Davis Antarctic station just east of Prydz Bay ($\sim 77^{\circ}$ E) between 1 and 5 January
98 2018 and featured nearly continuous high N_d clouds ($> 150 \text{ cm}^{-3}$) occurring in a
99 southerly flow passing over the ship that had trajectories from the Antarctic Continent.
100 Similarly, Twohy et al., (2021) report that the highest concentrations of aerosol
101 composed primarily of non-sea salt sulfates in the free troposphere north of 60° S
102 observed from research aircraft in Summer 2018 had occurred in airmasses that had
103 originated recently from over the Antarctic continent. See also Shaw et al. (1988) for an
104 early examination of the role of biogenic sulfate in modulating summertime aerosol
105 along coastal Antarctica. Shaw et al. (2007) expands on this idea as does Korhonen et
106 al., (2008).
107
108
109

110 2. Results

111
112 See Appendix A for methods and definitions. Approximately 40,000 1° latitude by 2°
113 longitude MBL cloud scenes per month meet our criteria for liquid phase non
114 precipitating clouds in the analysis domain. This number varies by $\sim 25\%$ in a seasonal
115 cycle that is due mostly to our solar zenith angle criteria. A seasonal cycle is evident in
116 the monthly-averaged cloud properties. LWP and r_e have seasonal minima in the
117 months of December and January. Due to an $r_e^{-5/2}$ dependence, N_d is of opposite phase
118 with r_e and correlated with it at -0.93. The seasonal variability in LWP (r_e) is on the
119 order of 7% (4%) and is small in comparison to N_d ($\sim 25\%$). τ and r_e are derived from
120 the visible and near infrared reflectances with the MODIS level 2 retrieval algorithm
121 (Nakajima and King, 1990). LWP is, then, calculated from
122

$$123 \quad \tau = \frac{3}{2\rho_w} \frac{LWP}{r_e} \quad (1)$$

124
125 that is derived in Stephens (1978). It is reasonable to consider whether seasonal
126 variations in N_d , perhaps linked to CCN, might be associated with variability in LWP.
127 We find that LWP decreases as N_d increases with a correlation coefficient in the
128 monthly means of -0.60.
129

130 In four of the five years, we see by inspection of Figure 1 that Chl-a leads changes in N_d
131 by approximately 1 month. The correlation coefficient of N_d and Chl-a increases from
132 0.27 to 0.60 when N_d is lagged from 0 to 1 month in the Figure 1 time series although
133 this result should be interpreted with caution given the break between February and
134 November in the time series. These results are broadly like those presented by McCoy
135 et al., (2015) and Mace and Avey (2017). McCoy et al. (2015) link N_d variations to PP

136 using regression analysis of MODIS derived N_d against a biogeochemical
 137 parameterization of biogenic sulfate and organic mass fraction (See also Lana et al.,
 138 2012).

139

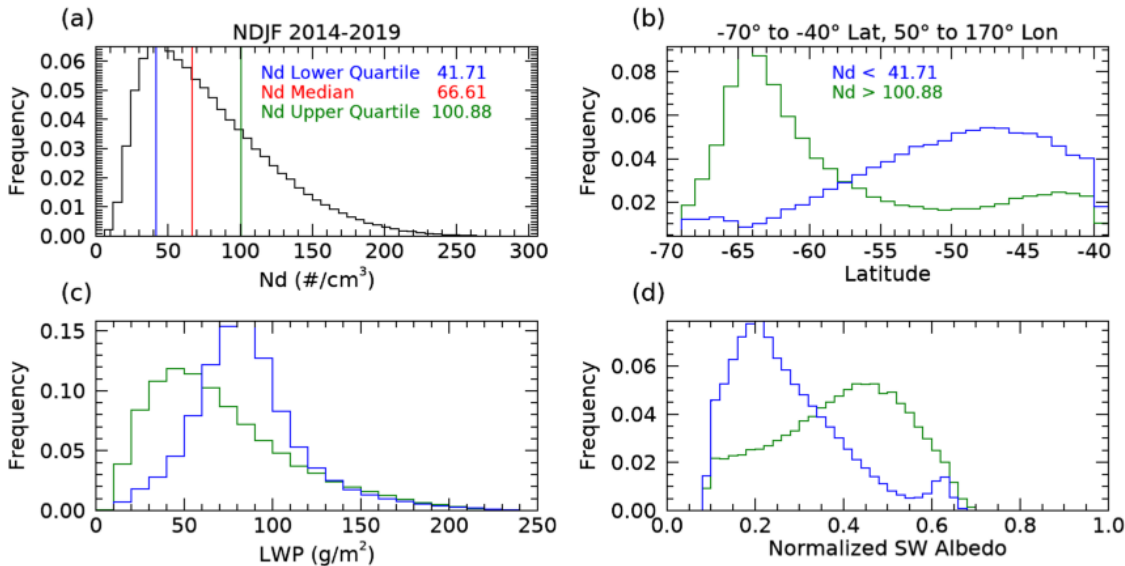


Figure 2. a) N_d frequency distribution from the cloud scenes in the analysis domain during the 5 years of summer months analyzed. Colored vertical lines are defined in the inset. b) The latitudinal distributions of the cloud scenes that compose the high and low N_d quartiles. c) the distributions of LWP for the high and low N_d quartiles, d) the distribution of normalized CERES solar albedo of the high and low N_d quartiles. The normalization procedure is described in the appendix. The colors of the histograms in panels b, c, and d, are as described in the inset of panel a.

140 We find a broad distribution of scene-averaged N_d (Figure 2a) with median, lower and
 141 upper quartile values of 66 cm^{-3} , 42 cm^{-3} and 101 cm^{-3} respectively. Henceforth, we
 142 focus our analysis on the groups of scenes that are less than and greater than the
 143 upper and lower quartiles. The high and low N_d scenes have distinct latitudinal
 144 occurrence distributions (Figure 2b) with low N_d scenes peaking broadly at 48°S while
 145 the high N_d scenes demonstrate a modal occurrence near 64°S . Overall, the N_d gradient
 146 implied by Figure 2 is correlated with the latitudinal distribution of imager-derived Chl-a
 147 (i.e., Deppler and Davidson, 2017). The seasonally averaged N_d gradient is also
 148 discussed in McCoy et al., (2020). Differentiating seasonally varying properties north
 149 and south of the ACFA (not shown), we find a clear differentiation in r_e and N_d with
 150 smaller r_e south of the ACFA (mean $r_e \sim 11 \text{ um}$, $N_d \sim 100$) compared to north (mean
 151 $r_e \sim 13 \text{ um}$, $N_d \sim 67 \text{ cm}^{-3}$). LWP is slightly larger by $\sim 7\%$ south of the ACFA. Both
 152 regions have a distinct seasonal cycle in cloud properties shown in Figure 1 although
 153 the southern latitudes have larger interannual variability likely owing to variations in
 154 annual sea ice extent and melt. The LWP distribution of the high N_d quartile is
 155 significantly shifted to lower values compared to the low N_d quartile LWP distribution

156 (Figure 2c). This finding is in accordance with the observational and theoretical work
157 presented in Glassmeier et al., (2021) who argue that closed cell stratocumulus that
158 dominate the clouds examined here have increased entrainment drying under higher N_d
159 conditions. Figure 2c and 2d illustrate that even though the high N_d quartile scenes tend
160 to have lower LWP, their solar albedo (A) tends to be significantly higher than the low
161 N_d quartile scenes illustrating the influence of cloud microphysics on the radiative
162 forcing of these clouds.

163
164 The high N_d scenes occur predominantly poleward of the ACFA (Figure 3). Interestingly
165 we find that the latitudinal gradient weakens slightly west of 90°E with a broad region of
166 higher N_d occurrence in the vicinity of the Kerguelen Rise where PP is higher (Cavagna
167 et al., 2015). Establishing causality between regions of high PP and cloud properties is
168 challenging (i.e., Meskhidze and Nenes, 2006; Miller and Yuter, 2008). While we find
169 seasonal associations over broad regions here, the chain of causality between
170 phytoplankton and clouds is not immediate or even necessarily direct because the
171 chemical processes take time to evolve and can move along chemical pathways that
172 have divergent outcomes (Woodhouse et al., 2013). To increase cloud N_d , new CCN
173 must be formed. Formation of new CCN can occur when sulfur compounds emitted
174 from the ocean surface nucleate after oxidation in the presence of sunlight. This
175 process of new particle formation occurs in the absence of other aerosol and often
176 requires mixing of the gaseous compounds from the boundary layer into the low-aerosol
177 free-troposphere where the newly formed aerosol can be transported widely (Shaw,
178 2007; Korhonen et al., 2008). Other pathways are possible such as deposition of
179 sulfate compounds onto primary sea salt particles that modify the chemical properties of
180 existing CCN rather than nucleating new CCN (Fossum et al., 2020) or even removal of

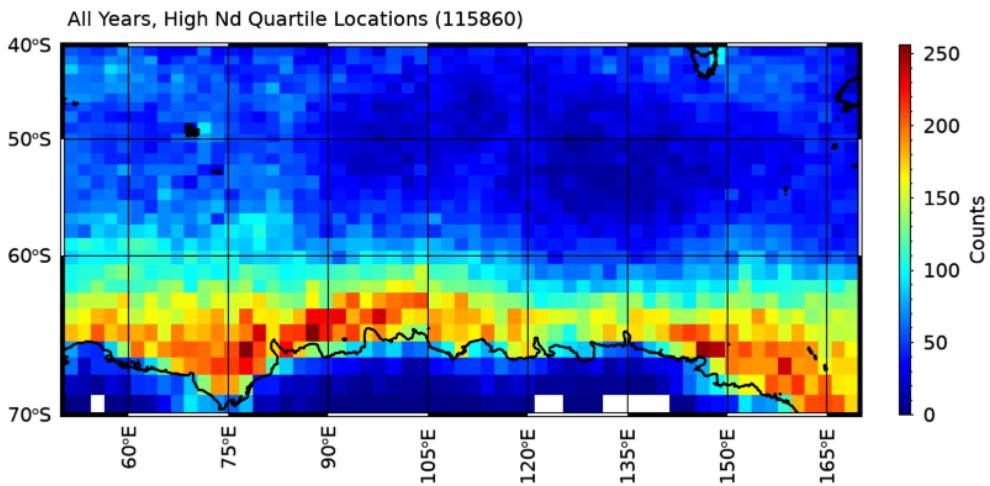


Figure 3. Geographic distribution of the high N_d quartile cloud scenes. Number in parentheses show the total of number cloud scenes from the 5-year summer data set.

181 sulfur compounds from the gas phase via aqueous phase oxidation in clouds
182 (Woodhouse et al., 2013).

183
184 Given the foregoing discussion, it seems reasonable that an airmass that is producing
185 clouds with certain features could be interacting with an aerosol population that has
186 evolved over periods of days (Brechtel et al., 1998). In addition, natural cloud
187 processes such as collision and coalescence of drops tend to cause N_d to decrease
188 while precipitation efficiently scavenges CCN, thereby lowering CCN concentration and
189 even modifying their composition and size through aqueous processing (Hoppel et al.,
190 1986). With larger r_e north of the ACFA, the collision-coalescence process is likely more
191 active (Freud and Rosenfeld, 2012) and could explain the latitudinal difference in
192 adiabaticity (see methods) found in in situ data. For instance, Kang et al. (2022)
193 analyzed data collected from Macquarie Island (54.6°S, 158.9°E) and found that, not
194 only were most clouds drizzling, but that precipitation as light as 0.01 mm hr⁻¹ could
195 reduce N_d by ~50%. Therefore, a cloud field should be considered as the product of
196 both local dynamics and thermodynamics primarily with modulation by a local
197 population of CCN. To examine the role of airmass history, we calculate the 5-day back
198 trajectories using the Hybrid Single-Particle Lagrangian Integrated Trajectory (HYSPLIT;
199 Stein et al., 2015) model using the Global Data Assimilation System (GDAS; Kamitsu,
200 1989) as input. The parcel's endpoint is the central latitude and longitude of the cloud
201 scene, and the location and model output are stored hourly.

202
203 South of the ACFA, the histories of the populations tend to be statistically different
204 (Figure 4). The low N_d clouds are more likely to be observed in airmasses that have
205 trajectories that originated in the open ocean region to the north of the ACFA. High N_d
206 scenes rarely evolve in airmasses that originate in the open ocean to the north of the
207 ACFA. The likelihood is that an airmass that has produced a high N_d cloud scene south
208 of the ACFA latitude has spent most of the previous 5 days over latitudes south of the
209 ACFA. North of the ACFA, the latitude distributions during the months of November and
210 February (not shown) are essentially identical for the high and low N_d quartiles.
211 However, for December and January, we find that the high N_d clouds observed north of
212 the ACFA have an increased likelihood of trajectories emanating from south of the
213 ACFA during the 5-days prior to the MODIS observation.

214
215 3. Discussion and Conclusions

216
217 Using MODIS level 2 cloud property retrievals and the technique developed in
218 Grosvenor et al. (2018; hereafter G18) to estimate N_d , we examine the latitudinal and
219 seasonal cycles of non-precipitating liquid-phase clouds in the Australasian sector of the
220 Summertime Southern Ocean. The r_e and N_d have distinctive differences north and
221 south of the ACFA but demonstrate similar seasonal cycles. We infer that the spatial
222 and temporal variability in cloud N_d , and r_e are at least partially a function of the
223 geographic and temporal variability in CCN that, in turn, is related to the seasonality of
224 primary sources such as sea salt and the latitudinal variability in marine PP. The
225 highest N_d clouds tend to be overwhelmingly found along the East Antarctic coastal
226 waters south of the ACFA.

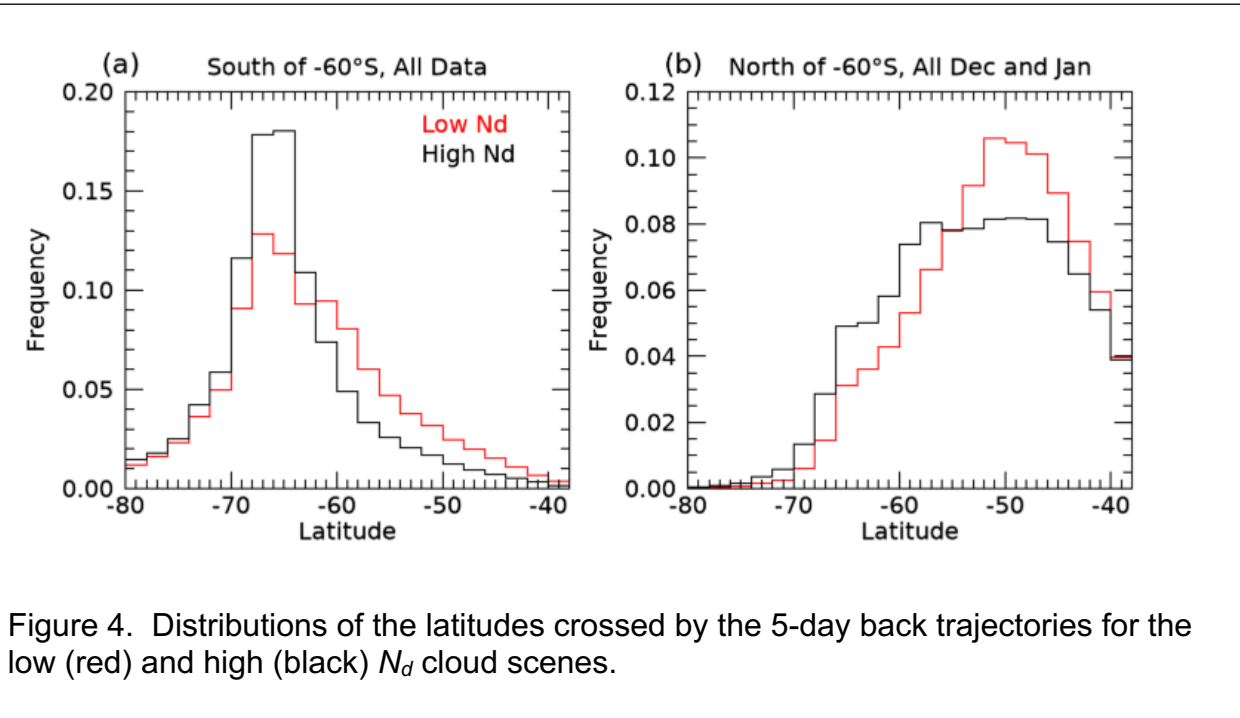


Figure 4. Distributions of the latitudes crossed by the 5-day back trajectories for the low (red) and high (black) N_d cloud scenes.

228 Because aerosol precursor gasses like DMS often require trajectories through the free
 229 troposphere to nucleate new particles that then take time to reach CCN sizes
 230 (Korohonen et al., 2008; Shaw et al. 2007), we examine the back trajectories of the
 231 airmasses observed with high and low N_d south of the ACFA and find significant
 232 differences. Low N_d cloud scenes are more likely to have arrived south of the ACFA
 233 from northerly trajectories that would have transported low CCN air dominated by sea
 234 salt. The high N_d cloud scenes are more likely to have trajectories that have remained
 235 adjacent to or had passed over the Antarctic continent. North of the ACFA, while the
 236 trajectory statistics for the high and low N_d quartiles in November and February are
 237 nearly identical, during December and January the high N_d clouds scenes tend to have
 238 an increased likelihood of arriving north of the ACFA from southerly trajectories,
 239 suggesting that high CCN airmasses are being transported northward especially during
 240 December and January.

241
 242 Given that the main difference between the source regions north and south of the ACFA
 243 is the magnitude of the marine PP, and given previous analyses of CCN compositional
 244 sensitivity to marine biological factors (e.g. Humphries et al., 2021; Vallina et al., 2006;
 245 Lana et al., 2012; McCoy et al., 2015), we conclude that the biological source of sulfate
 246 precursor gasses and the slackening of surface winds with latitude during Summer
 247 plays a dominating role in controlling the latitudinal gradients in the properties of weakly
 248 precipitating MBL cloud fields over the Southern Ocean. Figure 5 summarizes our
 249 findings by presenting composite seasonal cycles of MBL cloud scenes north and south
 250 of 60° S. The LWP in both latitudinal bands go through a weak seasonal cycle. The
 251 significant contrast in optical depth between the northern and southern bands is, we
 252 infer, mostly caused by the latitudinal contrast in N_d . Based on available evidence, we

253 conclude that the differences in r_e in MODIS retrievals are causally linked to oceanic PP
254 gradients that drive CCN, and thereby N_d , to be higher over the southern region. This
255 sensitivity, in turn, plays a significant role in modulating the regional albedo (A) and,
256 thereby, influences the input of sunlight to the surface ocean. We note that the
257 seasonal cycle in A is different between the northern and southern latitude domains (a
258 topic for future work), however, always A of the southern domain is higher than that of
259 the northern domain. However, we should be careful not to overstate this case. Cloud
260 processes that consume N_d and modify CCN (i.e. precipitation and cloud processing)
261 also play a role in modulating cloud N_d and therefore regional A (Kang et al., 2022;
262 McCoy et al., 2020). The airmass history and source region, while apparently
263 important, are among many factors involved.

264
265 Since the magnitude of PP is significantly lower north of the ACFA throughout the
266 summer season, a similar seasonal cycle in N_d and r_e suggests that CCN derived from
267 DMS oxidation of precursor gasses emitted primarily from Antarctic coastal waters
268 perhaps seeds much of the rest of the Southern Ocean with biogenic sulfate aerosol as
269 observed in recent airborne observations (Twohy et al., 2021). The northerly transport
270 of these high sulfate airmasses out of the Antarctic coastal waters (Figure 4b) and
271 southerly transport of low sulfate air masses into the Antarctic coastal region near the
272 surface (Figure 4a) have been reported by Humphries et al. (2016, 2021) and Shaw
273 (1988) and observed in the free troposphere with recent research aircraft
274 measurements (Twohy et al. 2021).
275

276 Our ability to identify natural marine cloud brightening (Latham et al., 2008) due to
277 aerosol-cloud coupling is a direct result of the absence of other anthropogenic and
278 continental influences in the pristine SO. As argued by McCoy et al. (2020), it seems
279 clear that in several important ways, the Southern Ocean is the last vestige of the
280 preindustrial atmosphere allowing us to constrain processes that remain important to
281 our understanding of the global climate (Carslaw et al., 2013).
282

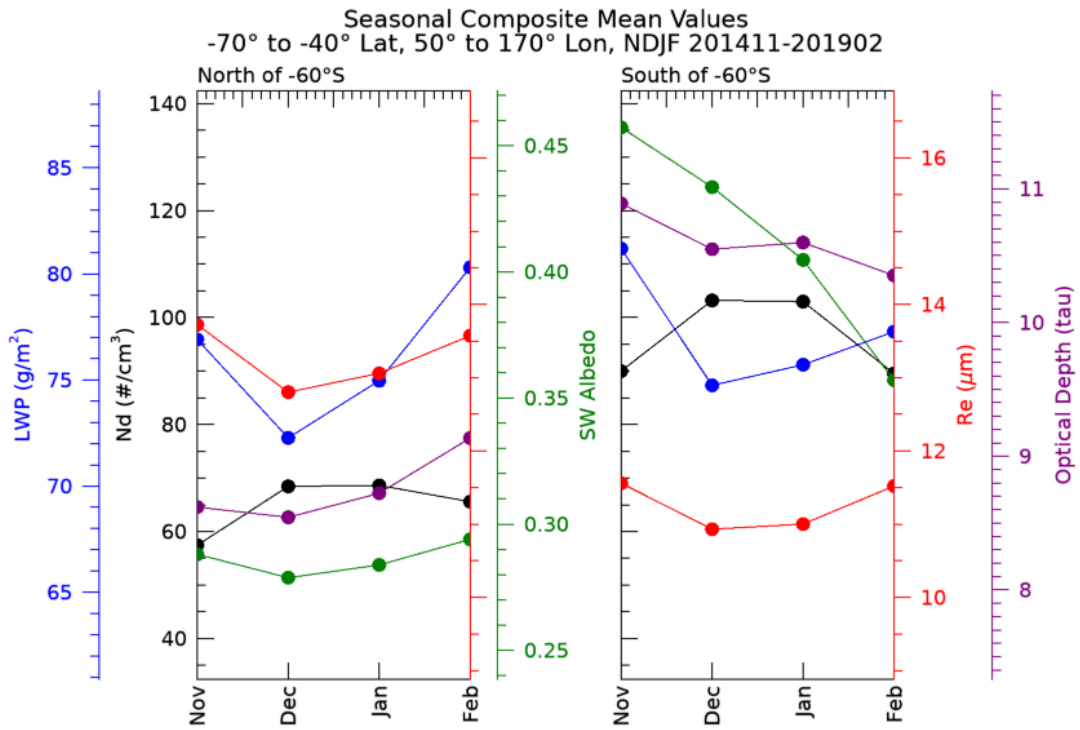


Figure 5. Composite seasonal cycle of cloud properties. Each data point is comprised of the monthly mean of cloud scenes in the analysis domain compiled from November 2014–February 2019. The effective radius (Re , red curve) and the optical depth (solid purple curve) are taken directly from MODIS Level-2 retrievals. The liquid water path (LWP, blue curve) and cloud droplet number (N_d , black curve) are derived as described in the text. The solar (SW) albedo (green curve) is derived from CERES data and normalized to a solar zenith angle of 45° as described in the Appendix.

283 Appendix. Methods

284

285 We use MODIS imager-derived Level-2 retrievals (Platnick et al., 2015) of effective
 286 radius (r_e) and optical depth (τ) from five summer periods (2014–2019) collected
 287 between the latitudes of 45°S and 76°S and longitudes of 40°E and 170°E to focus
 288 roughly on where the ships and aircraft sampled in Summer 2017–18. We calculate N_d
 289 using the method derived and evaluated in G18:

290

291

$$N_d = \frac{\sqrt{5}}{2\pi\kappa} \left(\frac{f_{ad} c_w \tau}{Q_{ext} \rho_w r_e^5} \right)^{1/2} \quad (\text{A1})$$

292

293 where ρ_w is the density of liquid water (1 g cm^{-3}), f_{ad} is an adiabaticity assumption, c_w is
 294 the vertical derivative of the adiabatic liquid water content, Q_{ext} is the extinction efficiency
 295 that is typically assumed to be 2 for cloud droplets, and κ is the cubed ratio of r_e to r_v . As

296 noted by G18, N_d depends on $r_e^{-5/2}$, which implies that the sensitivity or the rate of change
297 of N_d to retrieved r_e goes as the -7/2 exponent. Any biases in r_e , then would significantly
298 bias N_d . G18 provide a thorough evaluation of the sources of uncertainty in N_d due to
299 assumptions of adiabaticity, scene heterogeneity, etc., and conclude that N_d derived
300 using equation 1 applied to MODIS cloud retrievals has an overall uncertainty of ~80%.

301
302 The most uncertain quantity in the assumptions used in Equation A1 is f_{ad} since the cloud
303 vertical structure is not constrained by MODIS measurements. Using cloud thickness from
304 ship-based cloud radar and lidar along with retrieved LWP from collocated microwave
305 radiometer (Mace et al., 2021a), we estimate the value of f_{ad} in nonprecipitating
306 stratocumulus observed during the summer of 2018 (McFarquhar et al., 2021). We find
307 that the mean and standard deviation of f_{ad} north of the ACFA is 0.66 and 0.48,
308 respectively. South of the ACFA, the mean and standard deviation of f_{ad} is 0.93 and 0.60,
309 respectively. For the calculations of N_d in equation A1, we use a constant value for f_{ad} of
310 0.8. N_d is proportional to the square root of f_{ad} , therefore, $\frac{\partial \ln N_d}{\partial \ln f_{ad}} = \frac{1}{2}$ and a fractional
311 variation in f_{ad} on the order of 0.5 would imply an uncertainty in N_d of 0.25. Furthermore,
312 we expect in regions with f_{ad} higher (lower) than 0.8 the N_d would be biased low (high).
313 As we show, the regions with higher N_d tend be in the south and lower N_d in the north
314 counter to these expected biases. Additionally in this study, we will be examining
315 differences in spatially averaged N_d that are greater than a factor of 2. These results
316 imply that bias and random error due to uncertainty in f_{ad} is unlikely to significantly
317 influence the qualitative findings of this study.

318
319 Another source of systematic bias could be from the quantity κ that can be shown to be
320 a function of the variance of the droplet size distribution and is assumed to be a constant
321 at 0.7. G18 discusses this issue in some detail and concludes that there may be
322 systematic biases on the order of 12% that could be a function of N_d in pristine conditions.
323 While this quantity can be investigated with data collected in situ, no such data exists in
324 stratocumulus clouds south of the ACFA. Therefore, we recognize a potential source of
325 bias due to κ that is likely much smaller than the systematic latitudinal differences we find.
326

327 Given the uncertainties in N_d at the pixel level, we implement a filtering and averaging
328 scheme to focus on liquid phase, weakly precipitating cloud scenes. We define a scene
329 as a 1° latitude by 2° longitude domain where pixels are reported in the MODIS L2 data
330 to be of liquid-phase. We assume that clouds are weakly precipitating clouds if the cloud
331 liquid water path (LWP) < 300 g m⁻². We require that the sensor and solar zenith angles
332 (θ) at that pixel are less than 30° and 60°, respectively. The maximum θ requirement is
333 motivated by the findings of Grosvenor and Wood (2014) who find that systematic errors
334 in MODIS retrievals increase significantly for $\theta > 60^\circ$. The θ requirement causes us to
335 focus on the months from November through February. We require at least 1000 1-km
336 resolution pixels with these characteristics to exist within a scene (typical number
337 >10000). In addition, we require that no more than 10% of the pixels have a cloud top
338 temperature less than -20°C to ensure the absence of ice phase hydrometeors. Cloud
339 properties within a scene are averaged.
340

341 Collocated cloud albedos (A) of the cloud scenes are analyzed. A is derived from the
342 Clouds and the Earth's Radiant Energy System (CERES) Energy Balanced and Filled
343 (EBAF) version 4.0 (Loeb et al, 2018) data collected using instruments on board Aqua
344 and Terra. The albedo is derived by dividing the upwelling shortwave flux at the top of
345 the atmosphere (TOA) by the downwelling shortwave flux at TOA. Because A has a
346 solar zenith angle (θ) dependence, (Minnis et al. 1998), we normalize all albedo values
347 to $\theta=45^\circ$ (approximately the mean value of θ for the analysis domain and months
348 analyzed) with an empirical method using theoretically calculated A (\hat{A}) as a function of
349 latitude presented in Minnis et al. (1998 – their figure 7). The normalization is
350 implemented by first approximating the latitudinal dependence of A for various cloud
351 optical depths (τ) using the following regression equation: $\hat{A} = 0.51 - 0.43\mu_0^{1/2} +$
352 $0.17\ln\tau$ where $\mu_0 = \cos\theta$. \hat{A} approximates the variation of A with latitude within $\sim 15\%$
353 at $\tau=8$. The fit decreases in accuracy at higher and lower τ increasing to an uncertainty
354 of $\sim 30\%$ for $\tau=2$ and $\tau=32$ (these values of τ (2, 8, 32) are those presented in Minnis et
355 al., 1998, Figure 7). The averaged τ of the cloud scenes in our analysis is approximately
356 between 9 and 11 (Figure 5) so we expect that \hat{A} is typically a reasonable approximation
357 of A . The normalization of all A to $\theta = 45^\circ$ is accomplished by multiplying the CERES
358 A by the ratio $\frac{\hat{A}(\mu_0(\theta=45),\tau)}{\hat{A}(\mu_0,\tau)}$ where τ is from the MODIS cloud scene. The magnitude of the
359 ratio applied to the data ranges from 0.85 at higher latitudes to 1.2 at lower latitudes
360 with an average near 1.

361

362

363 Author Contributions: GM led the overall conception, data analysis of the study and
364 interpretation of the results. SB was responsible for implementing data analysis code
365 and generation of figures. RH provided background on aerosol chemistry and
366 processes. MPG and ES assisted GM in the study design and implementation.

367

368 Competing Interests: The authors declare no conflict of interest.

369

370 Acknowledgements: This work was supported by NASA Grant 80NSSC21k1969 and
371 DOE ASR Grants DE-SC00222001 and DE-SC0018995. All data used in this study are
372 available in public archives. MODIS cloud products can be found for Terra and Aqua at
373 <https://doi.org/10.5067/TERRA/MODIS/L3M/CHL/2018> and
374 http://dx.doi.org/10.5067/MODIS/MYD06_L2.006. Chlorophyl-a data are obtained from
375 Level 3 Standard Mapped Image Products available at MODIS
376 <https://doi.org/10.5067/AQUA/MODIS/L3M/CHL/2022>. Computer code for this study including
377 all analysis code and graphic generation code is written in the IDL language. Code is
378 available upon request to the corresponding author.

379

380 References

381

- 382 Arrigo, K. R., van Dijken, G. L., and Bushinsky, S.: Primary production in the Southern
383 Ocean, 1997–2006, *J Geophys Res*, 113, C8004,
384 <https://doi.org/10.1029/2007jc004551>, 2008.
- 385 Behrenfeld, M. J., Hu, Y., O’Malley, R. T., Boss, E. S., Hostetler, C. A., Siegel, D. A.,
386 Sarmiento, J. L., Schulien, J., Hair, J. W., Lu, X., Rodier, S., and Scarino, A. J.:
387 Annual boom–bust cycles of polar phytoplankton biomass revealed by space-
388 based lidar, *Nat Geosci*, 10, 118–122. <https://doi.org/10.1038/ngeo2861>, 2017.
- 389 Bodas-Salcedo, A., Hill, P. G., Furtado, K., Williams, K. D., Field, P. R., Manners, J. C.,
390 Hyder, P., & Kato, S.: Large Contribution of Supercooled Liquid Clouds to the
391 Solar Radiation Budget of the Southern Ocean, *J Climate*, 29, 4213–4228,
392 <https://doi.org/10.1175/jcli-d-15-0564.1>, 2016.
- 393 Brechtel, F. J., Kreidenweis, S. M., and Swan, H. B.: Air mass characteristics, aerosol
394 particle number concentrations, and number size distributions at Macquarie
395 Island during the First Aerosol Characterization Experiment (ACE 1), *J Geophys
396 Res-Atmos*, 103, 16351–16367, <https://doi.org/10.1029/97jd03014>, 1998.
- 397 Carslaw, K. S., Lee, L. A., Reddington, C. L., Pringle, K. J., Rap, A., Forster, P. M.,
398 Mann, G. W., Spracklen, D. V., Woodhouse, M. T., Regayre, L. A., and Pierce, J.
399 R.: Large contribution of natural aerosols to uncertainty in indirect forcing,
400 *Nature*, 503, 67–71, <https://doi.org/10.1038/nature12674>, 2013.
- 401 Cavagna, A. J., Fripiat, F., Elskens, M., Mangion, P., Chirurgien, L., Closset, I.,
402 Lasbleiz, M., Florez-Leiva, L., Cardinal, D., Leblanc, K., Fernandez, C., Lefèvre,
403 D., Oriol, L., Blain, S., Quéguiner, B., and Dehairs, F.: Production regime and
404 associated N cycling in the vicinity of Kerguelen Island, Southern Ocean,
405 *Biogeosciences*, 12, 6515–6528, <https://doi.org/10.5194/bg-12-6515-2015>, 2015.
- 406 Deppeler, S. L. and Davidson, A. T.: Southern Ocean Phytoplankton in a Changing
407 Climate, *Frontiers in Marine Science*, 4, 40,
408 <https://doi.org/10.3389/fmars.2017.00040>, 2017.
- 409 Fossum, K. N., Ovadnevaite, J., Ceburnis, D., Preißler, J., Snider, J. R., Huang, R.-J.,
410 Zuend, A., and O’Dowd, C.: Sea-spray regulates sulfate cloud droplet activation
411 over oceans, *npj Climate and Atmospheric Science*, 3, 14,
412 <https://doi.org/10.1038/s41612-020-0116-2>, 2020.
- 413 Glassmeier, F., Hoffmann, F., Johnson, J. S., Yamaguchi, T., Carslaw, K. S., and
414 Feingold, G.: Aerosol-cloud-climate cooling overestimated by ship-track data,
415 *Science*, 371, 485-489, <https://doi.org/10.1126/science.abd3980>, 2021.
- 416 Gras, J. L. and Keywood, M.: Cloud condensation nuclei over the Southern Ocean: wind
417 dependence and seasonal cycles, *Atmos Chem Phys*, 17, 4419–4432,
418 <https://doi.org/10.5194/acp-17-4419-2017>, 2017.
- 419 Grosvenor, D. P. and Wood, R.: The effect of solar zenith angle on MODIS cloud optical
420 and microphysical retrievals within marine liquid water clouds, *Atmos Chem
421 Phys*, 14, 7291–7321, <https://doi.org/10.5194/acp-14-7291-2014>, 2014.
- 422 Grosvenor, D. P., Sourdeval, O., Zuidema, P., Ackerman, A., Alexandrov, M. D.,
423 Bennartz, R., Boers, R., Cairns, B., Chiu, J. C., Christensen, M., Deneke, H.,
424 Diamond, M., Feingold, G., Fridlind, A., Hünerbein, A., Knist, C., Kollias, P.,
425 Marshak, A., McCoy, D., Quaas, J.: Remote Sensing of Droplet Number
426 Concentration in Warm Clouds: A Review of the Current State of Knowledge and

- 427 Perspectives, Rev Geophys, 56, 409–453, <https://doi.org/10.1029/2017rg000593>,
428 2018.
- 429 Gryspeerdt, E., Goren, T., Sourdeval, O., Quaas, J., Mülmenstädt, J., Dipu, S.,
430 Unglaub, C., Gettelman, A., and Christensen, M.: Constraining the aerosol
431 influence on cloud liquid water path, Atmos Chem Phys, 19, 5331–5347,
432 <https://doi.org/10.5194/acp-19-5331-2019>, 2019.
- 433 Hoppel, W. A., Frick, G. M., and Larson, R. E.: Effect of nonprecipitating clouds on the
434 aerosol size distribution in the marine boundary layer, Geophys Res Letters, 13,
435 125–128, <https://doi.org/10.1029/gl013i002p00125>, 1986.
- 436 Hu, C., Feng, L., Lee, Z., Franz, B. A., Bailey, S. W., Werdell, P. J., and Proctor, C. W.:
437 Improving satellite global chlorophyll a data products through algorithm
438 refinement and data recovery, J Geophys Res-Oceans, 124, 1524–
439 1543, <https://doi.org/10.1029/2019JC014941>, 2019.
- 440 Huang, Y., Siems, S. T., Manton, M. J., Rosenfeld, D., Marchand, R., McFarquhar, G.
441 M., and Protat, A.: What is the Role of Sea Surface Temperature in Modulating
442 Cloud and Precipitation Properties over the Southern Ocean?, J Climate, 29,
443 7453–7476, <https://doi.org/10.1175/jcli-d-15-0768.1>, 2016.
- 444 Humphries, R. S., Keywood, M. D., Gribben, S., McRobert, I. M., Ward, J. P., Selleck,
445 P., Taylor, S., Harnwell, J., Flynn, C., Kulkarni, G. R., Mace, G. G., Protat, A.,
446 Alexander, S. P., and McFarquhar, G.: Southern Ocean latitudinal gradients of
447 cloud condensation nuclei, Atmos Chem Phys, 21, 12757–12782,
448 <https://doi.org/10.5194/acp-21-12757-2021>, 2021.
- 449 Humphries, R. S., Klekociuk, A. R., Schofield, R., Keywood, M., Ward, J., and Wilson,
450 S. R.: Unexpectedly high ultrafine aerosol concentrations above East Antarctic
451 sea ice, Atmos Chem Phys, 16, 2185–2206, <https://doi.org/10.5194/acp-16-2185-2016>, 2016.
- 453 Kang, L., Marchand, R. R., Wood, R., and McCoy, I. L.: Coalescence Scavenging
454 Drives Droplet Number Concentration in Southern Ocean Low Clouds, J
455 Geophys Res, 49, e2022GL097819, <https://doi.org/10.1029/2022GL097819>,
456 2022.
- 457 Kanamitsu, M.: Description of the NMC Global Data Assimilation and Forecast
458 System. Weather and Forecast, 4, 335–342, [https://doi.org/10.1175/1520-0434\(1989\)004<0335:dotngd>2.0.co;2](https://doi.org/10.1175/1520-0434(1989)004<0335:dotngd>2.0.co;2), 1989.
- 460 Korhonen, H., Carslaw, K. S., Spracklen, D. V., Mann, G. W., and Woodhouse, M. T.:
461 Influence of oceanic dimethyl sulfide emissions on cloud condensation nuclei
462 concentrations and seasonality over the remote Southern Hemisphere oceans: A
463 global model study, J Geophys Res, 113, D15204,
464 <https://doi.org/10.1029/2007JD009718>, 2008.
- 465 Krüger, O. and Graßl, H.: Southern Ocean phytoplankton increases cloud albedo and
466 reduces precipitation, Geophys Res Letters, 38, L08809,
467 <https://doi.org/10.1029/2011gl047116>, 2011.
- 468 Lana, A., Simó, R., Vallina, S. M., and Dachs, J.: Potential for a biogenic influence on
469 cloud microphysics over the ocean: A correlation study with satellite-derived
470 data, Atmos Chem Phys, 12, 7977–7993, <https://doi.org/10.5194/acp-12-7977-2012>, 2012.

- 472 Latham, J., Rasch, P., Chen, C.-C., Kettles, L., Gadian, A., Gettelman, A., Morrison, H.,
473 Bower, K., & Choularton, T.: Global temperature stabilization via controlled
474 albedo enhancement of low-level maritime clouds, Philos T R Soc A, 366, 3969–
475 3987, <https://doi.org/10.1098/rsta.2008.0137>, 2008.
- 476 Mace, G. G.: Cloud properties and radiative forcing over the maritime storm tracks of
477 the Southern Ocean and North Atlantic derived from A-train, J Geophys Res-
478 Atmos, 115, D10201, <https://doi.org/10.1029/2009jd012517>, 2010.
- 479 Mace, G. G. and Avey, S.: Seasonal variability of warm boundary layer cloud and
480 precipitation properties in the Southern Ocean as diagnosed from A-Train Data, J
481 Geophys Res-Atmos, 122, 1015–1032, <https://doi.org/10.1002/2016jd025348>,
482 2017.
- 483 Mace, G. G., Protat, A., and Benson, S.: Mixed-phase clouds over the Southern Ocean
484 as observed from satellite and surface based lidar and radar, J Geophys Res-
485 Atmos, 126, e2021JD034569, <https://doi.org/10.1029/2021jd034569>, 2021.
- 486 Mace, G. G., Protat, A., Humphries, R. S., Alexander, S. P., McRobert, I. M., Ward, J.,
487 Selleck, P., Keywood, M., and McFarquhar, G. M.: Southern Ocean cloud
488 properties derived from CAPRICORN and MARCUS data, J Geophys Res-
489 Atmos, 126, e2020JD033368, <https://doi.org/10.1029/2020jd033368>, 2021.
- 490 McCoy, D. T., Burrows, S. M., Wood, R., Grosvenor, D. P., Elliott, S. M., Ma, P.-L.,
491 Rasch, P. J., and Hartmann, D. L.: Natural aerosols explain seasonal and spatial
492 patterns of Southern Ocean cloud albedo, Science Advances, 1, e1500157,
493 <https://doi.org/10.1126/sciadv.1500157>, 2015.
- 494 McCoy, I. L., McCoy, D. T., Wood, R., Regayre, L., Watson-Parris, D., Grosvenor, D. P.,
495 Mulcahy, J. P., Hu, Y., Bender, F. A.-M., Field, P. R., Carslaw, K. S., and
496 Gordon, H.: The hemispheric contrast in cloud microphysical properties
497 constrains aerosol forcing, P Natl A Sci USA, 117, 18998–19006,
498 <https://doi.org/10.1073/pnas.1922502117>, 2020.
- 499 McFarquhar, G. M., Bretherton, C. S., Marchand, R., Protat, A., DeMott, P. J.,
500 Alexander, S. P., Roberts, G. C., Twohy, C. H., Toohey, D., Siems, S., Huang,
501 Y., Wood, R., Rauber, R. M., Lasher-Trapp, S., Jensen, J., Stith, J. L., Mace, J.,
502 Um, J., Järvinen, E., ... McDonald, A.: Observations of Clouds, Aerosols,
503 Precipitation, and Surface Radiation over the Southern Ocean: An Overview of
504 CAPRICORN, MARCUS, MCRE, and SOCRATES, B Am Meteorol Soc, 102,
505 E894-E928, <https://doi.org/10.1175/bams-d-20-0132.1>, 2021.
- 506 Meskhidze, N. and Nenes, A.: Phytoplankton and Cloudiness in the Southern Ocean,
507 Science, 314, 1419–1423, <https://doi.org/10.1126/science.1131779>, 2006.
- 508 Miller, M. A. and Yuter, S. E.: Lack of correlation between chlorophyll-a and cloud
509 droplet effective radius in shallow marine clouds, Geophys Res Letters, 35,
510 L13807, <https://doi.org/10.1029/2008gl034354>, 2008.
- 511 Minnis, P., Garber, D.P., Young, D. F., Arduini, R. F., Takano, Y.: Parameterizations of
512 Reflectance and Effective Emittance for Satellite Remote Sensing of Cloud
513 Properties. J Atmos Sci, 55, 3313-3339, [https://doi.org/10.1175/1520-0469\(1998\)055%3C3313:PORAE%3E2.0.CO;2](https://doi.org/10.1175/1520-0469(1998)055%3C3313:PORAE%3E2.0.CO;2), 1998.
- 515 MODIS Characterization Support Team (MCST): MODIS Geolocation Fields Product.
516 NASA MODIS Adaptive Processing System, Goddard Space Flight Center, USA,
517 <http://dx.doi.org/10.5067/MODIS/MOD03.061>, 2017.

- 518 Naud, C. M., Booth, J. F., and Del Genio, A. D.: The Relationship between Boundary
519 Layer Stability and Cloud Cover in the Post-Cold-Frontal Region, *J Climate*, 29,
520 8129–8149, <https://doi.org/10.1175/jcli-d-15-0700.1>, 2016.
- 521 Painemal, D., Chiu, J.-Y. C., Minnis, P., Yost, C., Zhou, X., Cadeddu, M., Eloranta, E.,
522 Lewis, E. R., Ferrare, R., and Kollias, P.: Aerosol and cloud microphysics
523 covariability in the northeast Pacific boundary layer estimated with ship-based
524 and satellite remote sensing observations, *J Geophys Res-Atmos.*, 122, 2403-
525 2418, <http://doi.org/10.1002/2016JD025771>, 2017.
- 526 Platnick, S., Ackerman, S., King, M., et al.,: MODIS Atmosphere L2 Cloud Product
527 (06_L2), NASA MODIS Adaptive Processing System, Goddard Space Flight
528 Center, USA, http://dx.doi.org/10.5067/MODIS/MOD06_L2.061, 2015.
- 529 Shaw, G. E.: Do biologically produced aerosols really modulate climate?, *Environ Chem*
530 4, 382-383, <https://doi.org/10.1071/EN07073>, 2007.
- 531 Shaw, G. E.: Antarctic aerosols: A review, *Rev Geophys*, 26, 89–112,
532 <https://doi.org/10.1029/RG026i001p00089>, 1988
- 533 Stein, A. F., Draxler, R. R., Rolph, G. D., Stunder, B. J., Cohen, M. D., and Ngan, F.:
534 NOAA's HYSPLIT Atmospheric Transport and Dispersion Modeling System, *B
535 Am Meteorol Soc*, 96, 2059–2077, <https://doi.org/10.1175/bams-d-14-00110.1>,
536 2015.
- 537 Stephens, G. L.: Radiation Profiles in Extended Water Clouds. II: Parameterization
538 Schemes, *J Atmos Sci*, 35, 2123–2132, [https://doi.org/10.1175/1520-0469\(1978\)035.2123:RPIEWC.2.0.CO;2](https://doi.org/10.1175/1520-0469(1978)035.2123:RPIEWC.2.0.CO;2), 1978.
- 539 Trenberth, K. E. and Fasullo, J. T.: Simulation of Present-Day and Twenty-First-Century
540 Energy Budgets of the Southern Oceans, *J Climate*, 23, 440–454,
541 <https://doi.org/10.1175/2009jcli3152.1>, 2010.
- 542 Twohy, C. H., and Anderson, J. R: Droplet nuclei in non-precipitating clouds:
543 composition and size matter, *Environ Res Lett*, 3, 045002,
544 <https://doi.org/10.1088/1748-9326/3/4/045002>, 2008.
- 545 Twohy, C. H., DeMott, P. J., Russell, L. M., Toohey, D. W., Rainwater, B., Geiss, R.,
546 Sanchez, K. J., Lewis, S., Roberts, G. C., Humphries, R. S., McCluskey, C. S.,
547 Moore, K. A., Selleck, P. W., Keywood, M. D., Ward, J. P., and McRobert, I. M.:
548 Cloud-nucleating particles over the Southern Ocean in a changing climate,
549 *Earth's Future*, 9, e2020EF001673, <https://doi.org/10.1029/2020ef001673>, 2021.
- 550 Vallina, S. M., Simó, R., and Gassó, S.: What controls CCN seasonality in the Southern
551 Ocean? A statistical analysis based on satellite-derived chlorophyll and CCN and
552 model-estimated OH radical and rainfall, *Global Biogeochem Cy*, 20, GB1014,
553 <https://doi.org/10.1029/2005gb002597>, 2006.
- 554 Woodhouse, M. T., Mann, G. W., Carslaw, K. S., and Boucher, O.: Sensitivity of cloud
555 condensation nuclei to regional changes in dimethyl-sulphide emissions, *Atmos
556 Chem Phys*, 13, 2723–2733. <https://doi.org/10.5194/acp-13-2723-2013>, 2013.
- 557
- 558
- 559